Early-time hydrodynamic response of a tin droplet driven by laser-produced plasma

Javier Hernandez-Rueda [1], Bo Liu [1,2], Diko J. Hemminga [1,2], Yahia Mostafa [1,2], Randy A. Meijer [1,2],
Dmitry Kurilovich [3], Mikhail Basko [4], Hanneke Gelderblom [5], John Sheil [1,2] and Oscar O. Versolato [1,2,*]

[1]*Advanced Research Center for Nanolithography, Science Park 106, 1098 XG Amsterdam, Netherlands*
[2]*Department of Physics and Astronomy, and LaserLaB, Vrije Universiteit Amsterdam, De Boelelaan 1081, 1081 HV Amsterdam, Netherlands*
[3]*ASML Netherlands B.V., De Run 6501, 5504 DR Veldhoven, Netherlands*
[4]*Keldysh Institute of Applied Mathematics, Miusskaya Square 4, 125047 Moscow, Russia*
[5]*Department of Applied Physics, Eindhoven University of Technology, Den Dolech 2, 5600 MB Eindhoven, Netherlands*

We experimentally and numerically investigate the early-time hydrodynamic response of tin microdroplets driven by a ns-laser-induced plasma. Experimentally, we use stroboscopic microscopy to record the laser-induced dynamics of liquid tin droplets and determine the propulsion speed (U) and initial radial expansion rate ($\dot{R}_0$). The ratio of these two quantities is a key parameter to be optimized for applications in nanolithography, where laser-impacted tin droplets serve as targets for generating extreme ultraviolet light. We explore a large parameter space to investigate the influence of the tin droplet diameter, laser beam diameter, and laser energy on the $\dot{R}_0/U$ ratio. We find good agreement when comparing the experimentally obtained U and $\dot{R}_0$ values to those obtained by detailed radiation-hydrodynamic simulations using RALEF-2D. From the validated simulations, we extract the spatial distribution of the plasma-driven pressure impulse at the droplet-plasma interface to quantify its influence on the partitioning of kinetic energy channeled into propulsion or deformation. Our findings demonstrate that the width of the pressure impulse is the sole pertinent parameter for extracting the kinetic energy partitioning, which ultimately determines the late-time target morphology. We find good agreement between our full radiation-hydrodynamic modeling and a generalized analytical fluid-dynamics model [H. Gelderblom *et al.*, J. Fluid Mech. **794**, 676 (2016)]. These findings can be used to optimize the kinetic energy partition and tailor the features of tin targets for nanolithography.

I. INTRODUCTION

Today, state-of-the-art nanolithography machines employ liquid tin microdroplets as mass-limited targets to generate extreme ultraviolet (EUV) light, which is then used to produce semiconductor devices with unprecedented spatial resolution [1–5]. In this context, the generation of EUV light is based on a two-step process, where a first laser pulse (prepulse) shapes an initially spherical droplet into a thin layer of tin (target) [6]. This target is then illuminated by a second pulse (main pulse) to produce a dense and hot tin plasma, where several of its charge states (Sn^{10+}–Sn^{14+}) preferentially emit EUV radiation with a wavelength centered around 13.5 nm [7–12]. A full understanding and control of the (prepulse) laser-induced tin droplet dynamics over different timescales is key to optimize EUV source operation [13–17].

The interaction of a nanosecond laser prepulse with a spherical tin microdroplet can be separated into three main phases: (i) the initial laser-tin interaction and plasma generation and expansion on a nanosecond timescale, followed by (ii) an early deformation of the droplet lasting hundreds of nanoseconds and a subsequent (iii) fluid dynamic response of the system on a microsecond timescale, where surface tension plays a central role in shaping the target morphology. The characteristic times of these stages are illustrated on a logarithmic timeline in Fig. 1(a); more details of the timescale separation can be found in Refs. [18–20]. During the *first stage*, the laser-tin interaction drives the generation of a plasma whose rapid expansion imprints a pressure impulse at the droplet-plasma interface, radially expanding the droplet and propelling it along the laser propagation direction. The initial expansion rate $\dot{R}_0$ and the ballistic propulsion velocity U are on the order of 100 m/s [18–23]. Any plasma onset effects are short, on the hydrodynamic timescale $\tau_h \sim 0.1$–1 ns [18,19,24], much shorter than the laser pulse duration τ_p, so $\tau_h \ll \tau_p$ such that an ablation front is established providing plasma pressure over the full $\tau_p \sim 10$ ns timescale. In the *second stage*, the droplet starts to deform into a circular thin sheet. This early deformation takes place during the inertial time $\tau_i = R_0/\dot{R}_0 \sim 100$ ns, for a droplet radius $R_0 \sim 10$ μm. As deformation progresses toward the *third stage*, a rim forms at the periphery of the sheet, where surface tension causes a deceleration of the sheet's radial expansion rate on the capillary timescale $\tau_c = \sqrt{\rho D_0^3/(6\sigma)} \sim 10$ μm, with the droplet diameter D_0, the liquid density $\rho = 6900$ kg m^{-3}, and the surface tension $\sigma = 0.55$ N/m [18–20,22,23,25,26]. The surface tension drives the radial contraction of the sheet and fluid
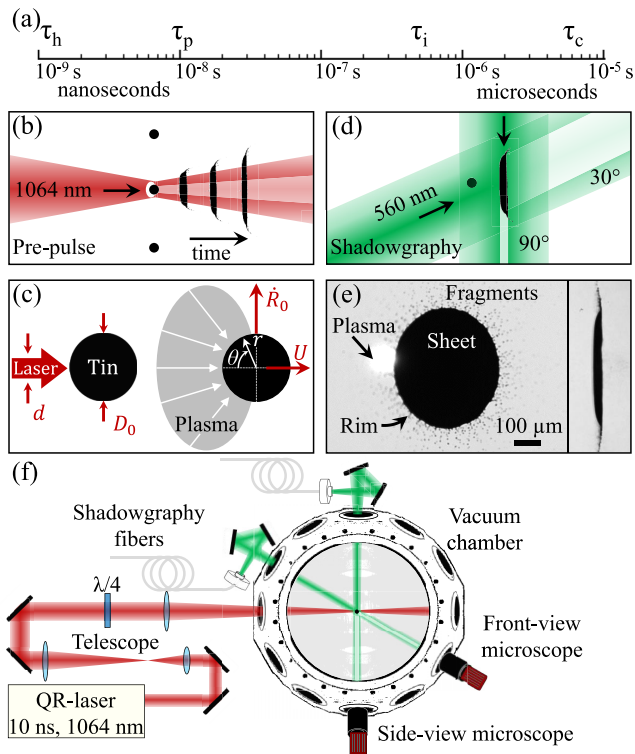
*o.versolato@arcnl.nl

FIG. 1. Schematics of laser-tin droplet interaction. (a) Characteristic times during and after the laser-droplet interaction. (b) Schematic of the irradiation geometry (side view). A liquid tin microdroplet is irradiated using a single focused ns-laser beam. The black circles represent the tin droplets and the elongated shadows illustrate the expanding tin target. (c) Schematic of the laser-droplet system with the most relevant parameters, including the laser beam d and droplet D_0 diameters and the propulsion U and radial $\dot{R}_0$ velocities. The cartoon on the right-hand side illustrates the momentum transfer to the droplet mediated by the laser-induced plasma expansion recoil. The cartoon also shows the polar coordinate system (r, θ) with its origin at the droplet center. (d) Schematic representation (top view) of the shadowgraphy illumination at $30°$ and $90°$ used to image the deforming droplet target. (e) Experimental front-view (left) and side-view (right) shadowgraphy images of a expanding sheet of tin. (f) Schematic of the top view of the experimental system.

dynamic instabilities both on the sheet [23,27] and at the rim [26,28]. The instabilities at the rim, in turn, form ligaments that eventually shed fragments via pinch-off processes [26,27]. Given the complexity of this dynamic deformation process, controlling the $\dot{R}_0/U$ ratio is crucial to tailor the precise target morphology. In an industrial setting, a specific target size is obtained by expanding at a rate $\dot{R}_0$ over a preset time interval. In this context, the propulsion speed U can be identified as a side effect from obtaining $\dot{R}_0$, essentially a loss channel of kinetic energy. Therefore, it is highly relevant to elucidate the physics that dictates how much of the deposited laser energy is channeled to radial deformation kinetic energy $E_{k,d}$ and forward propulsion kinetic energy $E_{k,cm}$ of tin targets and enable optimization thereof [20].

To understand the kinetic energy partitioning in the current problem, we can draw upon well-established analogies with

droplet impact upon a rigid substrate, where the impact velocity U is identified as the characteristic speed to describe the hydrodynamic response and sets the kinetic energy as the initial condition of the process [25,29–34]. However, in the classical case of drop impact onto a pillar, the late hydrodynamic response may further depend on the initial expansion rate $\dot{R}_0$ of the droplet, which deviates from U when varying the relative size of the drop with respect to the pillar diameter [25,35,36]. In the case of droplets irradiated by pulsed lasers (be it vapor-propelled water [18] droplets or plasma-propelled tin droplets [19]), there is no rigid body and instead the impact process is governed by the laser-matter interaction, which requires a more complex description of the mechanisms involved in the impact. The relation between a predefined pressure pulse and the fluid dynamic response of a droplet has been analytically described in Ref. [20]. In that work, the initial velocity field inside a droplet was derived by considering inviscid and incompressible flow after applying an instantaneous pressure impulse at a liquid droplet surface. In Ref. [20], the full hydrodynamic response (early and late stages) is then solely and fully determined by the ratio of kinetic energy initially channeled to deform the droplet and the kinetic energy to propel its center of mass. Although this work established a solid link between the partitioning of kinetic energy $E_{k,d}/E_{k,cm}$ in the droplet and a given analytical (and instantaneous) pressure impulse, a detailed description and understanding of the pressure impulse generated by the expanding plasma cloud itself is lacking. Moreover, the validity of the aforementioned assumptions (i.e., instantaneous, inviscid, incompressible) remain to be ascertained for the current, rather extreme case of a laser-impacted tin droplet.

In this work, we combine experiments and radiation-hydrodynamics simulations to investigate the ns-laser-induced early-time fluid dynamic response of liquid tin microdroplets. First, we experimentally record the evolution of the liquid tin morphology using stroboscopic shadowgraphy, from which we extract both the propulsion velocity U and expansion velocity $\dot{R}_0$. We systematically investigate the influence of the droplet diameter D_0, beam diameter d, and laser energy E on U and $\dot{R}_0$. The experimental U and $\dot{R}_0$ velocities agree well with those obtained from radiation-hydrodynamic simulations performed with the RALEF-2D code. The simulations further allow us to extract the pressure impulse at the droplet-plasma interface. We identify the width of the pressure impulse as the crucial characteristic length governing the kinetic energy partitioning $E_{k,d}/E_{k,cm} = f(\sigma)$. Thus, we elegantly describe the balance of kinetic energy channeled to the deformation or propulsion of the droplet using a single parameter that comprises the effect of all the experimental parameters: d, D_0, and E. Finally, this energy partition is compared with the predictions of a purely fluid dynamic model developed in Ref. [20].

II. EXPERIMENT

Figure 1(b) illustrates the tin droplet irradiation geometry, where a single laser prepulse illuminates a tin microdroplet. The recoil pressure exerted by the expansion of the laser-produced plasma gives rise to a propulsion and a radially symmetric deformation characterized by the center-of-mass

velocity U and the radial velocity $\dot{R}_0$, as shown in Fig. 1(c). In the current experiments, these velocities are on the order of 100 m/s. To study the expansion and propulsion dynamics, we use a stroboscopic shadowgraphy system as depicted in Fig. 1(d). This system provides front- and side-view images as a function of the time between the laser prepulse and the shadowgraphy probe pulse. In Fig. 1(e) we provide an example of shadowgraphy images and illustrate the main constituents of the expanding tin target.

A. Experimental setup

In the following, we explain the experimental system illustrated in Fig. 1(f); more details can be found in Ref. [37]. A vertical train of spherical liquid tin droplets (260 °C) is dispensed using a piezoelectric-driven droplet generator, which is mounted on a motorized assembly that adjusts the direction of the train. Its repetition rate ranges from 5 kHz to 65 kHz, which allows for accurate control of the droplet diameter D_0 from 55 μm to 25 μm. The droplets have a speed of 11 m/s while they pass through the center of a vacuum vessel (10^{-7} mbar). The droplets are illuminated using a light sheet generated by a He-Ne laser combined with a cylindrical lens. The scattered light is collected by a photomultiplier tube, down-converted to 10 Hz and used to trigger a Nd:YAG laser and the imaging systems.

For the laser experiments, we use a Nd:YAG laser system (Quanta-Ray, Spectra-Physics) that delivers linearly polarized pulses at a central wavelength of 1064 nm, with a repetition rate of 10 Hz. The laser has a Gaussian temporal profile with a pulse duration of $\tau_p = 10$ ns (FWHM). From this point forth, we simply refer to the prepulse laser as a laser. The laser passes through a quarter-wave plate to attain circular polarization at the droplet surface, which allows us to attain cylindrical symmetry of the laser energy deposition at the surface of the droplets, thus leading to an axisymmetric expansion. We use two telescopes to provide beam diameters of either 1 or 4 cm before passing through our focusing optics. We then focus the laser beam using a lens with a focal distance of 300 mm and a diameter of 7.5 cm. The full width at half maximum (FWHM) of the focused laser beam at the droplet location was adjusted in the range 15–130 μm by carefully modifying the position of the lens. The 1 cm and 4 cm input beam diameters enable us to scan ranges of 40–130 μm and 15–50 μm, respectively. Before the laser-tin interaction experiments, the laser Gaussian spatial distribution was characterized using a beam profiler by recording images of the attenuated laser beam while changing the distance between the lens and the center of the vacuum chamber. These images were used to characterize the beam diameter and the laser energy fraction impinging on the droplet surface.

The laser-induced dynamics of the irradiated droplets were recorded using a stroboscopic shadowgraphy imaging system. This system uses incoherent light pulses at 560 nm with a pulse duration of 5 ns to illuminate the expanding tin target by imaging it onto the chip of a CCD camera using a long-distance microscope (K2 Distamax, Infinity). Two twin shadowgraphy systems are used to record the dynamics at 30° (front view) and 90° (side view) with respect to the laser beam propagation axis. These imaging systems provide a spatial
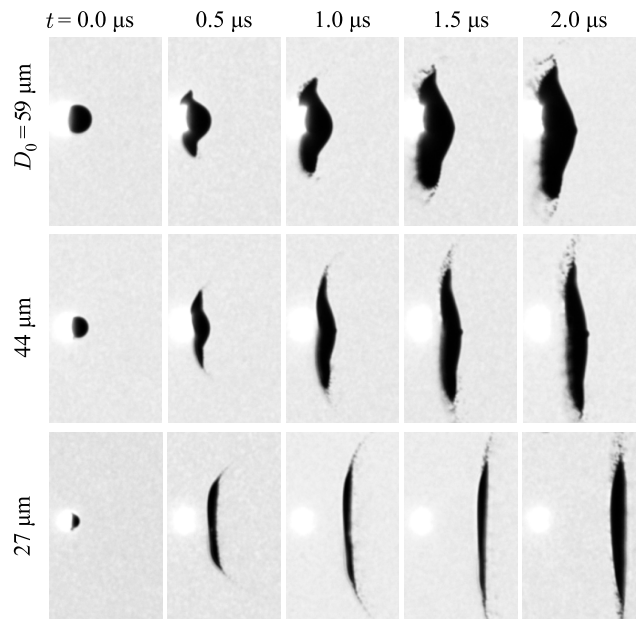

FIG. 2. Set of representative side-view shadowgraphy images. Each image illustrates the target morphology considering different droplet diameters (rows) and time delay after laser illumination (columns). Note that the laser beam propagates from left to right in the images and thus impinges on the left side of the droplets. Here, we set $d = 20$ μm and $E = 0.8$ mJ. The bright spot in all images corresponds to the laser-induced plasma emission. The images capture an area of 425 μm by 270 μm.

resolution of 5 μm. The time delay between the prepulse laser and the shadowgraphy pulses was set to start at $t = -500$ ns extending up to 4000 ns.

B. Experimental results

In the following, we will examine the laser-induced target morphology, propulsion speed U and the initial expansion rate $\dot{R}_0$ of the droplet and their dependence on the variables of E, d, and D_0 for a large parameter space. The droplet response is also influenced by the polarization state [38] and the temporal intensity distribution of the laser [39,40], which we set to be constant here.

1. Target morphology

In Fig. 2, we show a set of representative shadowgraphy images of the expanding tin target at several time delays (columns). These images illustrate a variety of morphologies that are the result of irradiating droplets with three different diameters (D_0 rows), while keeping a constant laser beam diameter and energy ($d = 20$ μm and $E = 0.8$ mJ). The ablation of smaller droplets leads to flatter tin morphologies forming an axisymmetric thin sheet (see bottom row with $D_0 = 27$ μm). For larger droplets, morphologies with a smaller radius of curvature are observed. This curved morphology is caused by a nonhomogeneous (but cylindrically symmetric) laser energy deposition at the droplet surface, as the beam is much smaller than the droplet and a certain area of the droplet surface remains unaltered. The top row exemplifies

this effect, where the beam diameter ($d = 20$ μm) is approximately one third of the droplet diameter $D_0 = 59$ μm. This case shows a partial ablation of the droplet surface around its pole, which resembles the ablation of a flat liquid pool as it generates a similar crown-shaped splash [41]. In contrast, the bottom row illustrates an experiment where the whole left hemisphere of the droplet is illuminated by the laser and, therefore, is ablated more homogeneously.

In addition to the morphology, the shadowgraphy images in Fig. 2 illustrate a change in propulsion speed and expansion rate when varying the droplet size. This becomes evident when comparing the sheet positions at $t = 2$ μs (rightmost column) between the $D_0 = 59$ μm and $D_0 = 27$ μm cases, where a faster propulsion speed for smaller, and thus lighter, droplets is observed. Furthermore, smaller droplets exhibit a faster initial expansion rate, which can be seen by comparing the sheet diameters at $t = 0.5$ μs for different droplet sizes. Next, we will quantitatively explore the propulsion and expansion rates and their dependence when varying E, d, and D_0.

2. Laser-induced propulsion of liquid tin droplets

The acceleration of the droplet to a center-of-mass velocity U takes place in the short timescale of $\tau_p \sim 10$ ns, after which U remains constant. This velocity can be described by a function of several laser and geometrical parameters $U = f(d, D_0, E)$ as shown in Refs. [18,21,23]. Our current work explores this dependence for a much larger parameter space, in which we explicitly consider the case where the beam size is smaller than the droplet size $d < D_0$ (see full data sets provided in Appendix A). Figure 3 presents U as a function of E, D_0, and d as independent variables. The data indicate that the propulsion velocity increases with increasing laser energy in panel (a) and decreasing droplet (b) and beam diameters (c). These observations agree well with our previous study in Ref. [21], where the *energy-on-droplet* E_{od} was identified as the principal parameter determining U (considering a single D_0 value). The E_{od} is defined as the incident laser energy illuminating the droplet surface; i.e., it accounts for the geometrical overlap of the laser beam profile and the spherical droplet surface as

$$E_{od} = E\left(1 - 2^{-D_0^2/d^2}\right). \quad (1)$$

A power-law dependence of U with E_{od} has been established by Kurilovich *et al.* [21] as

$$U = K_U E_{od}^{\alpha}, \quad (2)$$

with $K_U = K_U'(50 \text{ μm}/D_0)^{1+2\alpha}$, where K_U' is a proportionality factor that does not depend on D_0 [21]. The exponent α originates from the correlation between the plasma pressure and the laser pulse intensity and was determined to be $\alpha = 0.6$ in Refs. [19,21]. Naturally, an increase in pulse energy leads to a higher E_{od}, which yields a higher propulsion velocity, as seen in Fig. 3(a). On the one hand, a larger droplet size increases the overlap with the incident beam, leading to a larger E_{od} and to a larger impulse exerted by the plasma pressure. On the other hand, the mass of the droplet and hence the momentum corresponding to a certain propulsion velocity increases
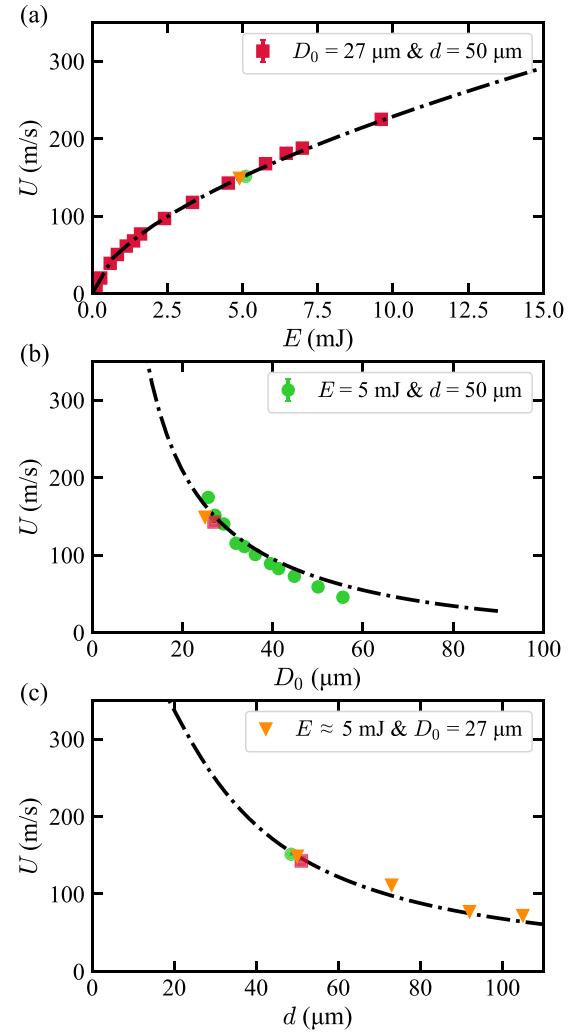

FIG. 3. Experimental center-of-mass velocity U. Graphs of U as function of (a) the laser energy E, (b) droplet diameter D_0, and (c) beam diameter d. In (a), the droplet and beam diameters were set to $D_0 = 27$ μm and $d = 50$ μm, respectively. In (b), the beam diameter and the energy were set to $d = 50$ μm and $E = 5$ mJ. In (c), the droplet diameter and the energy were set to $D_0 = 27$ μm and $E \approx 5$ mJ. In all graphs the dash-dotted lines are the result of a global fit of Eq. (2) to the data. Overlapping symbols are horizontally offset for visibility.

following $P \sim D_0^3 U$. As a result, the propulsion velocity is expected to decrease with droplet size, which is consistent with our observations in Fig. 3(b). As for the beam size, a tightly focused beam, while keeping a constant E-D_0 combination, leads to a higher E_{od}, which therefore results in a larger U as shown in panel (c). Equation (2) is then fitted to our data in Fig. 3 with (a) E, (b) d, and (c) D_0 as independent variables. We perform a global fit to all data in Fig. 3 with the power α fixed to 0.6 while leaving K_U' as a free fitting parameter. The fit yields a sole prefactor equal to $K_U' = 41(5)$ m s^{-1} mJ$^{-0.6}$, which agrees well with a value $K_U' = 36(3)$ m s^{-1} mJ$^{-0.6}$ obtained in Refs. [19,21]. The specified uncertainty is dominated by the error in characterizing the beam diameter d at the location of the droplet. Moreover, the global fit shown here is consistent with the fit presented in Fig. 8(a) in Appendix A,

which also yields $K'_U = 41 \text{ m s}^{-1} \text{mJ}^{-0.6}$. In Fig. 8(a), Eq. (2) is fitted to the combined U, E_{od} data that collapse onto a single curve for seven beam diameters that scale from 17 μm up to 100 μm.

Our study validates the applicability of Eq. (2) over a wide range of d-D_0-E combinations including the case where the laser focus is smaller than the droplet. For the case of $d < D_0$ we have no grounds to assume that the coefficient K_U is a function of D_0 only, and one should explicitly account for the dependence on d as well. In this case the imparted momentum would scale with d^2, following the intersecting beam-droplet area. However, the precise scaling is influenced by (i) the reduction of the fraction of propelled mass, as a result of employing a beam size that is smaller than the droplet ($d < D_0$), and (ii) plasma expansion from the illuminated droplet area, increasing the intersecting beam-plasma absorption area (see the following discussion in Sec. III). Our results suggest that these effects compensate divergence in this $d < D_0$ case from the momentum scaling $P \sim D_0^2$ found in the $d > D_0$ case [21]. We emphasize here that the propulsion velocity U can be elegantly determined by $U = f(E_{od}, D_0)$ with all data shown to collapse onto a single curve; see Fig. 8 in Appendix A. Such an independence of U on the beam size, when E_{od} and D_0 are given, however, is not applicable to define the initial expansion rate $\dot{R}_0$, as we discuss in Sec. II B 3.

3. Expansion dynamics of liquid tin droplets

The ns-laser-induced expansion dynamics of liquid tin microdroplets has been studied previously in Refs. [20,22,25,27,28]. As discussed in Sec. I, these works established how the radial trajectory $R(t)$ can be well described on a microsecond timescale by fluid-dynamics models in analogy to a droplet-pillar impact case that considers incompressible flow. After a rapid radial acceleration due to the impulse imparted by the impact, the droplet primarily deforms into a thin sheet delimited by a rim. The radial expansion hence undergoes an initial laser-driven acceleration and a subsequent deceleration due to the surface tension. In this way, the radius of the sheet increases, at an initial expansion rate of $\dot{R}_0$, reaches a maximum radius, and then contracts. The maximum sheet size and the expansion trajectory $R(t)$ are determined by the deformation Weber number $We_d = \rho D_0 \dot{R}_0^2 / \sigma$ with the liquid density $\rho = 6900 \text{ kg m}^{-3}$ and the surface tension $\sigma = 0.55 \text{ N/m}$ [18,23]. In Fig. 4(a), the radius of the sheet $R(t)$ as a function of time is plotted for several combinations $E, d,$ and D_0, which all lead to the same propulsion velocity of $U = 80 \text{ m/s}$. We choose data sets with the same U in order to discuss the origin of different expansion-to-propulsion ratios. Our data clearly illustrate (i) the initial radial expansion of the sheet and (ii) the effect of the surface tension that causes the gradual decrease of the expansion rate leading to the observation of an apex radius and a subsequent decrease of $R(t)$.

Figure 4(b) presents the dimensionless sheet radius $(R - R_0)/R_0 \sqrt{We_d}$ following Villermaux *et al.* [25], using the deformation Weber number We_d [27], as a function of the scaled time t/τ_c. Considering the droplet sizes used in the experiments (27 μm and 45 μm), we obtain capillary
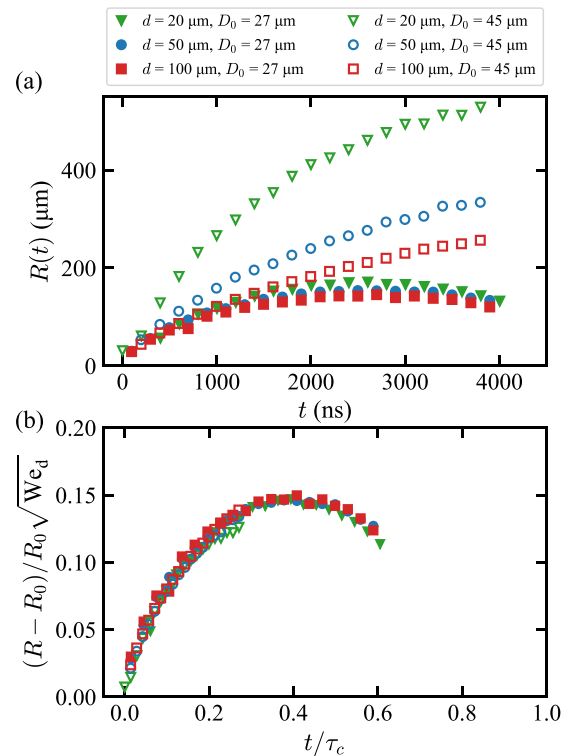

FIG. 4. (a) Sheet radius $R(t)$ from experiment as a function of time. These experiments were performed using three beam diameters and two droplet diameters while keeping a constant propulsion velocity of 80 m/s. (b) Dimensionless sheet radius $(R - R_0)/R_0 \sqrt{We_d}$ as a function of the time relative to the capillary time τ_c. Open and solid markers indicate results for tin droplet diameters of 45 μm ($E_{od} \approx 2.8 \text{ mJ}$) and 27 μm ($E_{od} \approx 0.3 \text{ mJ}$), respectively.

times of 5.7 μs and 12.2 μs, respectively. Figure 4(b) shows that all the data collapse onto a single curve upon use of the scaled parameters. Such a collapse is consistent with the findings reported in Refs. [20,25,42].

As mentioned above, the initial expansion rate $\dot{R}_0$ has been identified as a crucial variable to characterize the fluid dynamic response that dictates the radial expansion. Therefore, we limit our analysis here to $\dot{R}_0$, which is obtained by a linear fit to the $R(t)$ data up to $t = 300 \text{ ns}$. In analogy to $U(E_{od}, D_0)$ in Eq. (2), we first seek an expression of the form $\dot{R}_0 = f(E_{od}, D_0)$. A quantitative study of the response of a droplet to laser impact for various laser parameters, but keeping U constant (see Fig. 4 and also Appendix A), shows that unlike the propulsion speed U, there is an additional, explicit dependence of $\dot{R}_0$ on the beam size d, and thus, $\dot{R}_0 = f(E_{od}, D_0)$ is not complete. As predicted in Ref. [20], experiments performed using a tighter focused beam result in a larger $\dot{R}_0$. This effect can be seen in Fig. 4(a) by comparing the data obtained by using beam sizes $d^\nabla = 20 \text{ μm}$ and $d^\square = 45 \text{ μm}$, where $\dot{R}_0^\nabla > \dot{R}_0^\square$ for equal U.

The nontrivial dependence of $\dot{R}_0$ on the laser beam size d and its relevance to explain the fluid dynamic response inspired us to numerically investigate the plasma pressure and its spatial profile at the droplet surface. In the next section, we will discuss the precise way in which momentum is transferred at the plasma-droplet interface through the use of radiation-hydrodynamic simulations.

III. SIMULATION

A. Code description

We have performed simulations of the laser-droplet interaction and subsequent droplet deformation and expansion using the two-dimensional (2D) radiation-hydrodynamic RALEF (Radiation Arbitrary Lagrangian-Eulerian Fluid dynamics) code [43,44]. The code was originally developed to model high-temperature laser-plasma experiments conducted at GSI Darmstadt [45,46]. In more recent times, however, the application domain of the code has shifted to the modeling of laser-driven tin plasmas in the context of EUV light sources for nanolithography [10,21,24,47–49].

The hydrodynamic module of RALEF-2D is based on an upgraded version of the 2D CAVEAT code developed at Los Alamos National Laboratory [50]. The code solves the single-fluid single-temperature hydrodynamic equations on a structured quadrilateral mesh using a second-order Godunov-type scheme; see Ref. [17] for more details. Algorithms for thermal conduction and radiation transport have been implemented using the symmetric semi-implicit method with respect to time discretization [51,52]. Energy transport via thermal radiation is described by the quasistatic LTE (local thermodynamic equilibrium) radiation transport equation [24], and its solution is obtained using the method of short characteristics [53]. The angular dependence of the radiation intensity is modeled using the S_n quadrature method with $n = 6$ [54]. In order to obtain a solution of the LTE radiation transfer equation, one must have information on the radiative properties, i.e., the *spectral absorption coefficients* of the plasma. These data were generated with the THERMOS code [55,56] and are imported into RALEF-2D in tabular format. For a given density-temperature (ρ, T) pair, the THERMOS code solves the system of collisional-radiative level population equations (in steady-state equilibrium) from which the spectral absorption coefficients are obtained. These data are discretized into 28 spectral groups for use in the simulations. The equation-of-state (EOS) of tin was obtained from the Frankfurt EOS (FEOS) package [57] which is based on the original QEOS model [58] and is an extension of the MPQeos code [59]. A very attractive feature of the FEOS model is its ability to model the low-temperature liquid-gas phase coexistence regions, which is enabled through fully equilibrium calculations with Maxwell's construction in the two-phase region. We note that the code does not take into account the effects of surface tension, whose influence during the early expansion phase is negligible considering that $\tau_i \ll \tau_c$.

We performed two sets of simulations for spherical tin droplets having diameters $D_0 = 27$ μm and 45 μm. Our simulations were performed in the axisymmetric (z, r) geometry, where the symmetry axis of the tin sheet coincides with the laser propagation direction and passes through the center of the initially spherical droplet. As detailed in Ref. [21], we construct a polar coordinate system with its origin at the initial position of the droplet center. We adopted a detailed mesh structure of 1 mm radius exhibiting 360 zones over the π interval of the polar angle θ (defined with respect to the z axis pointing toward the incoming laser direction; see Fig. 1(c) and Ref. [21]). The mesh is progressively refined toward the initial droplet surface such that the thickness of the outermost

cell is approximately 10 nm. The initial density of the liquid tin targets was set to $\rho_0 = 6900$ kg m^{-3}. The region outside the droplet was filled with a low-density tin vapor having $\rho = 10^{-7}$ kg m^{-3}. In the simulations, we employed a $\lambda = 1064$ nm laser pulse with a Gaussian temporal profile with $\tau_p = 10$ ns (FWHM). For both droplet diameter cases, simulations were performed with Gaussian laser beams with FWHM diameters $d = 20, 30, 50$, and 100 μm. The laser beam employed in the simulations was unpolarized. Laser light propagation and absorption in the plasma was treated using a hybrid model accounting for the effects of laser reflection and refraction in the corona of plasma [60]. The simulations were run up to a time $t_f = 300$ ns, where the center-of-mass speed has become insensitive to the choice of t_f. We note here that we do not adjust any parameters within our simulations to reproduce the experimental observations.

B. Simulation results

1. Numerical validation: Droplet propulsion and the expansion speed

In this section, we will validate our simulations by comparing the propulsion speed U and the radial expansion rate $\dot{R}_0$ from RALEF-2D to the values determined in our experiments. The determination of U from the RALEF-2D simulations is straightforward and follows that outlined in Ref. [21]. This quantity is defined as the velocity of the center of mass (comprising all material having a density greater than 1000 kg m^{-3}) 300 ns after the laser pulse is switched on in the simulations. In Fig. 5(a) we present the U values as a function of E_{od}. The black dashed line corresponds to a fit of Eq. (2) (with $\alpha = 0.6$) to all the obtained experimental data with a droplet size $D_0 = 45$ μm (see Fig. 8 in Appendix A). The symbols represent the RALEF-2D predictions for laser beam diameters $d = 20$ (green hexagons), 30 (brown diamonds), 50 (blue squares), and 100 (red triangles) μm, respectively. The simulated data clearly follow the power-law dependence established in the experimental data.

The evaluation of the radial expansion velocity $\dot{R}_0$ from the RALEF-2D simulations is more complicated than that of U, mainly due to the difficulties in defining the liquid density at the boundary of the droplet and therefore $R(t)$ over time. From the simulations we extracted the radius that corresponds a density of (i) $\rho_{th}^u = 100$ kg m^{-3} and (ii) $\rho_{th}^d = 1000$ kg m^{-3}. We extracted the value of $R(t)$ every 10 ns within the time interval $100 \leqslant t \leqslant 300$ ns. We then fitted a linear function to the $R(t)$ data, from which $\dot{R}_0$ was obtained.

In Fig. 5(b) we plot the experimental observations and RALEF-2D predictions for $\dot{R}_0$ as a function of E_{od}. The upper bound $\dot{R}_0$ simulated data correspond to a $\rho_{th}^u = 100$ kg m^{-3} reference density and the lower bound data points correspond to $\rho_{th}^d = 1000$ kg m^{-3}. It is clear that the largest spread in simulated $\dot{R}_0$ values is attributed to the $d = 20$ μm case, where best agreement with experimental data can be found for the $\rho_{th}^d = 1000$ kg m^{-3} reference density. With increasing beam diameter, this spread is observed to decrease. An interesting behavior is observed for the $d = 50$ μm case where the experimental data predict a higher radial expansion velocity than both reference densities. Overall, our simulation results of U
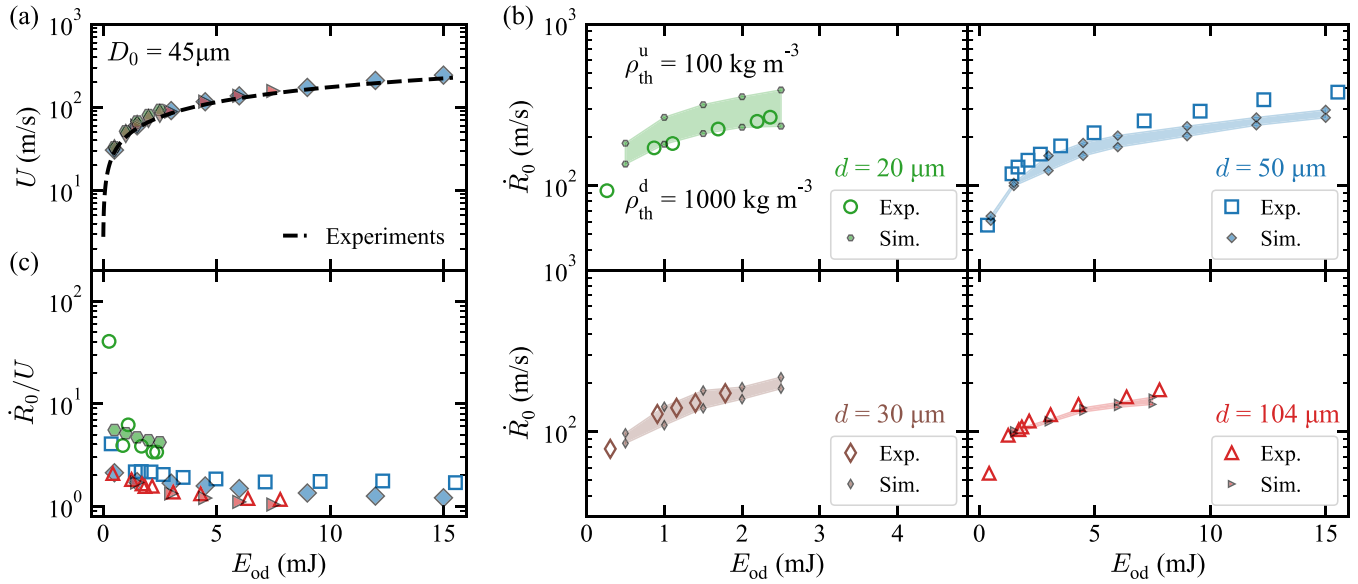
FIG. 5. Comparison between experiments and simulations. In the $D_0 = 45$ μm case, the filled and empty markers represent the simulation and experimental results, respectively. Graphs of (a) the propulsion velocity, (b) the initial radial velocity, and (c) the ratio $\dot{R}_0/U$ as a function of $E_{\rm od}$. In (a) the dashed line represents the fit of the experimental data presented in Fig. 8(b). The shaded areas in panel (b) present the estimated $\dot{R}_0$ ranges using RALEF-2D, where the upper and lower limits correspond to the values calculated using density thresholds of 100 and 1000 kg m^{-3}, respectively.

and $\dot{R}_0$ are in good to excellent agreement with our experimental findings, as shown in Figs. 5(a)–5(b). Moreover, the $\dot{R}_0/U$ ratios in panel (c), calculated for several example cases, are also in good agreement with the experiments considering the reference density $\rho_{th}^d = 1000$ kg m^{-3}. We note that this ratio is larger than 1 in all instances. This good agreement validates the capability of RALEF-2D in simulating the laser-droplet impact under the current numerical settings, which emulate the experimental conditions in this study. Next, we will present numerical results on the pressure profile.

2. Pressure impulse distributions

As discussed above, the recoil pressure exerted by the expanding plasma imparts forward momentum, P, to the droplet and hence sets the propulsion and expansion behavior. The plasma pressure is related to the forward momentum obtained by the target through

$$P = \int_0^{t_f} \iint_A p_a(t, \theta) \, \mathbf{e}_z \cdot d\mathbf{A} dt, \tag{3}$$

where $p_a(t, \theta)$ is the plasma pressure at the droplet surface as a function of time t and polar coordinate θ [20]. We define the local impulse as the time integral of the local pressure $j_p(\theta) = \int_0^{t_f} p_a(t, \theta) dt$, which is therefore only a function of angle. This integration ends at 95 ns [61]. We note that 90% of the full pressure impulse is imparted within ~10 ns from the time at which the peak intensity of the laser pulse is achieved, which is set to 15 ns in this work. The momentum imparted to the droplet thus can be described by the spatial shape of $j_p(\theta)$ [61]. Figures 6(a)–6(d) illustrate profiles of the normalized pressure impulse $\bar{j}_p(\theta) = j_p(\theta)/j_p(0)$ at the droplet-plasma interface, where $j_p(0)$ corresponds to the pressure impulse at the droplet pole $\theta = 0°$. These profiles are associated with two droplet sizes, namely $D_0 = 45$ and 27 μm. We seek the

dependence of $j_p(\theta)$ on the droplet size D_0, beam size d, and energy-on-droplet $E_{\rm od}$.

Figures 6(a) and 6(b) present $j_p(\theta)$ profiles for increasing beam sizes d, with a constant $E_{\rm od} = 1.5$ mJ. The top panels illustrate how tighter laser foci lead to narrower pressure impulse distributions; e.g., see the blue curve in Fig. 6(a) with $d = 50$ μm. This observation is expected as the ablation and the consequent plasma generation follow the local intensity of the incident beam [19,62]. We also observe that the irradiation of larger droplets, considering a constant beam size d, results in narrower impulse distributions, as shown for instance by comparing the blue curves in Figs. 6(a) and 6(b). The bottom panels (c) and (d) present graphs of $j_p(\theta)$ for increasing $E_{\rm od}$ values for a given beam size of $d = 20$ μm. Our data indicate that a higher $E_{\rm od}$ slightly broadens the pressure profile, creating a more uniform distribution. This is due to the faster expansion of the plasma (induced by the increased intensity), which wraps around the droplet, as was also reported in Refs. [21,39].

We use the data shown in Figs. 6(a)–6(d) to quantify the angular size of the pressure pulse at the droplet surface. We find that our data can be well described by a Gaussian distribution. This resemblance, along with the function employed in Gelderblom *et al.*, motivated us to fit a Gaussian function to our pressure curves as $j_p(\theta) = j_p(0) \exp[-\theta^2/(2\sigma^2)]$ [20]. The fits provide the angular size σ (i.e., standard deviation) of the pressure distributions that we later use to calculate the size of the arc at the droplet surface $\sigma \times D_0$. Following Ref. [20], this angular size sets the late-time target morphology. We illustrate examples of these fits to the orange profiles as dashed lines in Figs. 6(a)–6(d). Cosine-shaped pressure impulses, observed here for particularly large fluence cases in Fig. 6(d), constitute the limiting case in Ref. [20] projecting a flat momentum impulse
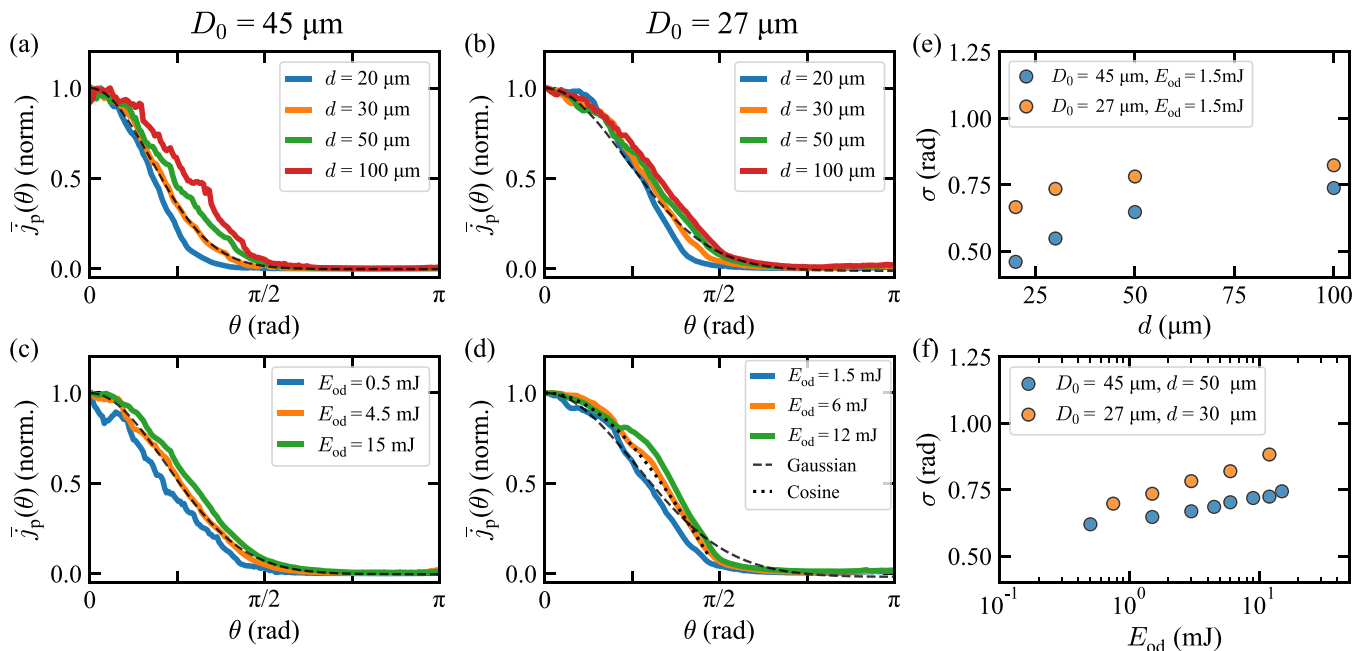
FIG. 6. Normalized pressure impulse at the surface of a tin droplet extracted from our RALEF-2D simulations. Graphs in panels (a) and (b) present results considering a constant $E_{od} = 1.5$ mJ and four beam sizes while the results in panels (c) and (d) consider constant beam sizes of $d = 50$ μm in (c) and in $d = 30$ μm (d) and three energy-on-droplet values. The simulations were performed for two droplet sizes $D_0 = 27$ and 45 μm. The dashed lines in (a)–(d) illustrate Gaussian fits that enable characterizing the angular size σ. For comparison purposes, the dotted line in (d) shows a fit to a cosine function. Graphs of the angular size σ extracted from the pressure impulse profiles as a function of the d and E_{od} are shown in (e) and (f), respectively.

distribution onto a spherical surface. Figures 6(e) and 6(f) show σ as a function of the beam size d and E_{od}, respectively. The data indicate wider pressure impulse profiles when using both a larger beam size and a higher energy-on-droplet, consistent with the aforementioned observation in panels (a)–(d).

IV. DISCUSSION

Thus far, we have seen how varying the droplet diameter D_0, beam size d, and laser pulse energy E will influence the droplet expansion speed $\dot{R}_0$ and the propulsion speed U. The magnitudes of these speeds, and their ratio, provide valuable insight into the balance of kinetic energy channeled either to the radial deformation, $E_{k,d}$, or to accelerating the center of mass of the droplet, $E_{k,cm}$. As mentioned in the Introduction, in Ref. [20], the energy ratio $E_{k,d}/E_{k,cm}$ was identified as the pertinent quantity to describe the late-time evolution of the droplet morphology, e.g., at times $t \sim \tau_c \sim$ μs. In Refs. [20,27] direct estimates of the energy partitioning were retrieved from experimentally obtained velocities by using the relation $E_{k,d}/E_{k,cm} \propto \dot{R}_0^2/U^2$ (also see Appendix B). The calculation of the prefactors that accompany this power law relation depends on the assumptions made about the late-time geometry of the target. For instance, a 1/2 prefactor results from considering a thin disk, i.e., a sheet of uniform thickness [20]. A 1/3 prefactor was obtained in Ref. [27] assuming a thickness $h \sim 1/(rt)$, following Ref. [25]. In reality, the sheet thickness changes in a more complex manner with the radial coordinate (over time) [23]. Even with a validated model of the late-time sheet thickness for the current case [23], no

reliable predictions for early-time morphology can be extrapolated from it and instead we use RALEF-2D to determine the early-time kinetic energies and their ratios and compare the results with the model from Ref. [20].

In our simulations, the total kinetic energy of the liquid body is determined by the sum of the discretized kinetic energies corresponding to each cell with a volume δV_i and a velocity vector $\mathbf{u}_i$,

$$E_k = \sum_i \frac{1}{2} \rho_i \, \delta V_i |\mathbf{u}_i|^2, \tag{4}$$

with the liquid body containing all tin with a density larger than 1000 kg m^{-3}, i.e., the reference density used for the center-of-mass speed U and expansion velocity $\dot{R}_0$ in Sec. III. Following Ref. [20], we identify the kinetic energy of the center of mass as

$$E_{k,cm} = \frac{1}{2} U^2 \left(\sum_i \rho_i \, \delta V_i \right), \tag{5}$$

also over a region with $\rho_i > 1000$ kg m^{-3}. Next, the *deformation kinetic energy* is defined as the remaining kinetic energy obtained when subtracting $E_{k,cm}$ from E_k, namely

$$E_{k,d} = E_k - E_{k,cm}. \tag{6}$$

The energy partitioning between the deformation and the propulsion of the droplet can thus be quantified by $E_{k,d}/E_{k,cm}$. Although we have shown that U can be described by a function that solely depends on E_{od} and D_0, $\dot{R}_0$ cannot, and is a function of E_{od}, D_0, and d. Therefore, we initially assume here that the energy partition follows $E_{k,d}/E_{k,cm} = f(E_{od}, D_0, d)$.
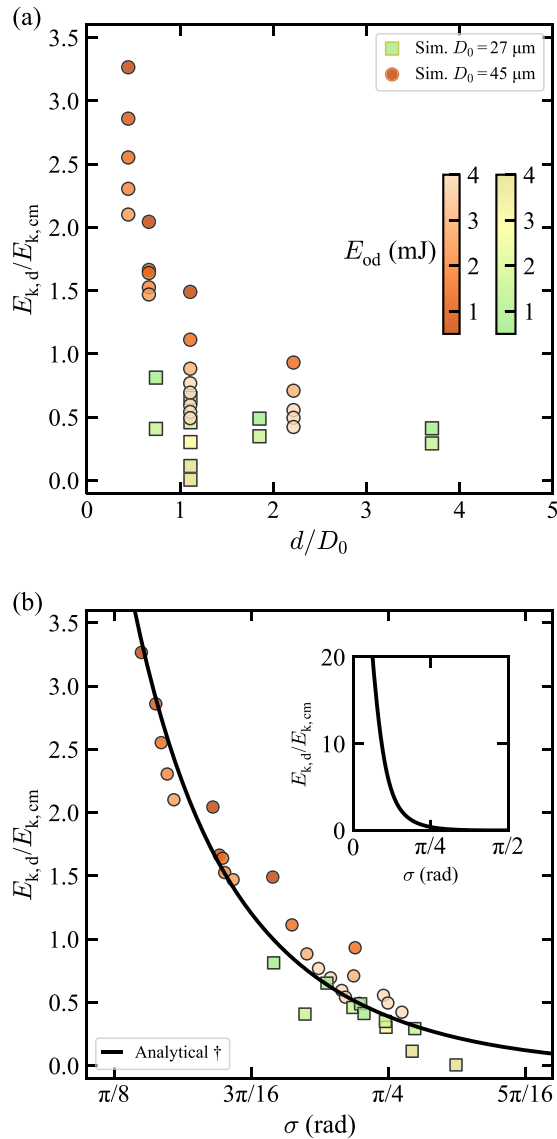
FIG. 7. Simulated kinetic energy partition. $E_{k,d}/E_{k,cm}$ as a function of (a) the size ratio d/D_0 and (b) the pressure impulse width σ. The black solid line † in (b) was calculated following the analytical expression proposed by Gelderblom *et al.* in Ref. [20].

We further seek a representative parameter that incorporates these three variables to simplify the expression for $E_{k,d}/E_{k,cm}$.

We first investigate the dependence of the energy partition on the beam-to-droplet size ratio d/D_0, the only *a priori* known dimensionless length scale in our system. Figure 7(a) shows $E_{k,d}/E_{k,cm}$ as a function of d/D_0, where data for two droplet sizes and multiple E_{od} (color bars) are presented. The graph illustrates that more tightly focused beams, with respect to the droplet size (i.e., smaller d/D_0), lead to a higher kinetic energy channeled to deform the droplet, $E_{k,d}$, instead of propelling it. This observation can be expected from Fig. 5(c) where $\dot{R}_0$ increasingly exceeds U when ever-smaller beams are employed. However, the beam-to-droplet size ratio d/D_0 cannot fully account for the effect of the E_{od} on the energy partition as illustrated in Fig. 7(a). Furthermore, it fails to capture the change in energy ratio comparing the

two droplet sizes for any pulse energy. We thus conclude that d/D_0 is not the pertinent length scale for the problem at hand.

In Fig. 6, we describe the pressure impulse $j_p(\theta)$ using a Gaussian function, which provides an angle σ and hence a characteristic arc length σD_0 for each d-D_0-E_{od} combination. This length defines the actual width of the pressure field at the droplet surface. According to Figs. 6(e)–6(f), for a given D_0, the width σD_0 increases with the size of the beam d and with the laser energy E_{od}. Therefore, the width of the pressure field σD_0 is a better choice of a characteristic length scale to determine the expansion response of the droplet as it comprises the effect of all experimental parameters.

Next, we describe the energy partition $E_{k,d}/E_{k,cm}$ as a function of σ, i.e., the ratio between the arc length of the pressure field and the droplet diameter $(\sigma D_0)/D_0 = \sigma$. Figure 7(b) presents $E_{k,d}/E_{k,cm}$ as a function of σ with the same data shown in panel (a). All the data fall onto a single curve, suggesting that σ is indeed the relevant dimensionless length scale, that simultaneously incorporates the effect of E_{od}, d, and D_0 on the energy partition. In this way, we simplify the expression of the kinetic energy partitioning to $E_{k,d}/E_{k,cm} = f(\sigma)$.

Reference [20] provides an analytical model that can predict the $E_{k,d}/E_{k,cm}$ ratio for any pressure impulse and studies in particular detail the response to a Gaussian-shaped pressure impulse. The close approximation of our $j_p(\theta)$ by a Gaussian function (see Fig. 6) hence enables our data to be directly compared to the results obtained from the fluid dynamic model using the very same definition of σ. This comparison is presented in Fig. 7(b), which shows an excellent agreement between our simulations and the model. We note that the most extreme cases, i.e., those with the largest σ values, correspond to scenarios where the dominant fraction of the initial droplet mass is ablated whereas the model assumes that a negligible mass fraction is ablated (for nonextreme cases this mass loss fraction is at the $\sim$10% level in line with Ref. [21]). At these large values of σ also the largest relative deviations between model and simulations are observed. These deviations should not be interpreted as a breakdown of the model, but instead as the limit of the range of validity of the current comparison. Considering the complexity of our RALEF-2D simulations, which include a plethora of physics aspects, the agreement shown between the simulation and the analytical model [20] is remarkable. This agreement validates the key model [20] assumptions of (i) an instantaneous pressure impulse causing an (ii) inviscid, (iii) incompressible flow. The assumption (i) is valid for the cases in the current work, where the liquid velocity field is established well before significant deformation occurs as $\tau_p \ll \tau_i$. The next model assumption (ii) of inviscid flow is valid as the typical Reynolds number is of order Re $\sim$ 10 000. Finally, assumption (iii) on incompressibility is partially validated in the present study. The fluid dynamic response of a droplet is dominated by incompressible flow when the $\tau_p/\tau_a \gg 1$ (the St number) and $p_a/\rho c_s^2 \ll 1$ (the Ma number) [61,63]. Here, $\tau_a = R_0/c_s$ is the acoustic time, which accounts for the time that an acoustic wave takes to travel half the droplet diameter at the speed of sound $c_s \sim 2500$ m/s [64]. In our current study, the pulse duration $\tau_p/\tau_a \approx 1$–2, which was shown in Ref. [40] to be sufficient to assure that the

flow is dominated by compressible flow. The plasma pressure p_a differential is indicated by our simulations to be smaller, at $\sim$100 kbar, than the base pressure of liquid tin at 430 kbar, thus satisfying the condition $p_a/\rho c_s^2 < 1$ to a sufficient degree.

The level of agreement between our simulations and the analytical theory [20] suggests that approximating $j_p(\theta)$ by the Gaussian function is indeed an appropriate measure to characterize the pressure impulse profile in our context. More importantly, the agreement indicates that the combined effect of laser ablation and the dynamics of the plasma impacting droplet can be captured by a single dimensionless quantity σ that uniquely sets the energy partition, which in turn [20] determines the late-time response of the droplet target. The droplet response to laser impact can be accurately described by the incompressible hydrodynamic response of an initially undeformed droplet to an instant pressure impulse. These findings assist in the robust prediction of final target morphology in industrial sources of EUV light.

V. CONCLUSION

In this paper, we investigated the early hydrodynamic response of liquid tin microdroplets upon nanosecond laser irradiation. Both experimental and numerical methods were employed to explore and understand the influence of the laser energy E, beam diameter d, and droplet diameter D_0 on the laser-induced dynamics of tin droplets. Experimentally, we recorded the expansion and propulsion of tin droplets using stroboscopic microscopy, which aids to determine the propulsion speed U and the initial radial expansion rate $\dot{R}_0$. Our results show that the irradiation of smaller droplets, while keeping constant E and d, leads to flatter morphologies and faster expansion and propulsion velocities, when compared to their larger counterparts. Moreover, we show how the propulsion velocity can be accurately described—for a large set of experiments with different E, d, and D_0 combinations—using a function of $U = f(D_0, E_{\mathrm{od}})$ that was introduced in Ref. [19] for a single D_0. Our results also reveal a more complex behavior of the radial expansion rate with an explicit dependence on the beam size $\dot{R}_0 = f(D_0, E, d)$.

To be able to predict and fully understand the dependence of $\dot{R}_0$ on E, d, and D_0 and its balance with U, we employed radiation-hydrodynamic simulations using RALEF-2D. The comparison between the experimental and numerical U and $\dot{R}_0$ results shows good agreement, which supports the validity of RALEF-2D in this context. In order to quantify the kinetic energy partition channeled to deform or propel laser-irradiated tin droplets, we retrieved the spatial distribution of the plasma-driven pressure $\bar{j}_p(\theta)$ at the droplet-plasma interface from our simulation. We found that $\bar{j}_p(\theta)$ profiles can be well approximated by a Gaussian function, from which we identify a dimensionless length scale σ to characterize the width of the pressure field.

The unique combination of experiments and simulations used here reveals that σ can be used as the sole relevant parameter to extract the kinetic energy partition $E_{\mathrm{k,d}}/E_{\mathrm{k,cm}}$

that further determines the target morphology on a microsecond timescale. Our description of the energy partition $E_{\mathrm{k,d}}/E_{\mathrm{k,cm}} = f(\sigma)$ using radiation-hydrodynamics modeling is in excellent correspondence with the generalized fluid-dynamics model of instantaneous pressure-driven droplet dynamics proposed by Gelderblom *et al.* [20]. These findings support the separation of characteristic timescales, reconciling the generation of the laser-driven pressure impulse (tens of nanoseconds) and the early hydrodynamic deformation during the inertial time τ_i (hundreds of nanoseconds). Following the conclusions from the here validated theoretical work [20], an optimized scheme for deforming a droplet without losing energy to propulsion is to employ the tightest possible laser focus. Naturally, any gains from such a scheme need to be balanced against increases in sensitivity to laser-to-droplet alignment as is elucidated in, e.g., Refs. [65,66]. Furthermore, the final morphology, which is uniquely set by the choice of σ [20], may impact the obtainable conversion efficiency of drive laser light into in-band EUV photons. Our results thus contribute to further the development of laser-driven plasma sources for EUV nanolithography by aiding to accurately attain the desirable features and morphology of tin targets.

APPENDIX A: SCALING OF U AND $\dot{R}_0$ WITH LASER ENERGY ON DROPLET

Figure 8 illustrates several panels with graphs of experimental U, $\dot{R}_0$, and $\dot{R}_0/U$ data as a function of the E_{od} for two different droplet diameters, namely $D_0 = 27$ μm (top panels) and 45 μm (bottom panels). In Figs. 8(a) and 8(b), we present a large set of experimental U-E_{od} curves for several beam diameters and two different droplet diameters. We find that the experimental data collapse onto a single U-E_{od} curve for a given droplet size. The black dashed lines illustrate fits to Eq. (2), which shows good agreement with the experimental observations when considering $\alpha = 0.6$ and $K_U' = 41$ m s^{-1} mJ$^{-0.6}$. In Figs. 8(c) and 8(d), we present the radial velocity $\dot{R}_0$ as a function of the E_{od}. As a reference, we also plot the fits obtained in panels (a) and (b) to illustrate that
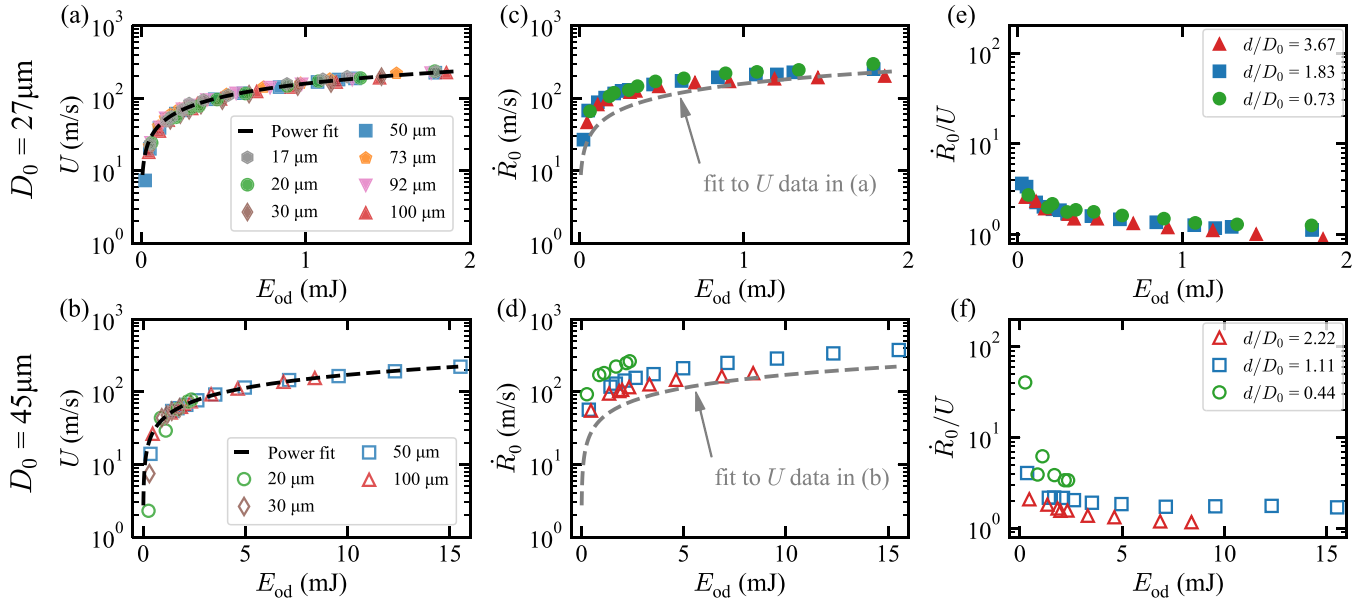
FIG. 8. Experimental $\dot{R}_0$ and U for a large variety of d-D_0-$E_{\rm od}$ combinations. Graphs of the experimental propulsion velocity U, (a) and (b), and the radial velocity $\dot{R}_0$, (c) and (d), as a function of the energy-on-droplet $E_{\rm od}$. The graphs on the top and bottom rows present the results that correspond to experiments carried out using two droplet diameters, namely $D_0 = 27\ \mu{\rm m}$ (filled markers) and $45\ \mu{\rm m}$ (empty markers), respectively. Different colors represent the data acquired using different beam diameters, ranging from $17\ \mu{\rm m}$ up to $100\ \mu{\rm m}$. The dashed lines are fits to the experimental data in (a) and (b) using Eq. (2). (e), (f) Ratio between the radial velocity and propulsion velocity as a function of the energy-on-droplet. Different colors represent data for several d/D_0 ratios as shown in the legend, which are consistent with the colors assigned to the beam diameters.

the radial velocity is in most cases larger than the propulsion velocity. We also observe that the $\dot{R}_0$-$E_{\rm od}$ curves do not overlap for the whole $E_{\rm od}$ range. Considering a constant D_0 and $E_{\rm od}$, the laser-induced radial velocity is larger when using a tightly focused beam than a loosely focused beam; see for instance the data markers near $E_{\rm od} = 2$ mJ in panels (c) and (d). We also note here that the differences in $\dot{R}_0$ are more pronounced for the $D_0 = 45\ \mu{\rm m}$ case. These observations confirm that the expansion velocity depends not only on D_0 and $E_{\rm od}$, like U, but also depends on the beam size d, as $\dot{R}_0 = f(D_0, d, E_{\rm od})$; see Sec. III B 1. Consequently, overall the $\dot{R}_0/U$ ratios are larger for a larger droplet size as shown in panels (e) and (f).

APPENDIX B: KINETIC ENERGY PARTITION VERSUS VELOCITY RATIO

Figure 9 presents the energy partition $E_{\rm k,d}/E_{\rm k,cm}$ obtained by RALEF-2D as a function of the velocity ratio $\dot{R}_0/U$. By assuming that the droplet ultimately deforms into a sheet with an uniform thickness, i.e., the velocity field of the liquid in the sheet linearly follows $u \sim r\dot{R}/R(t)$, Gelderblom *et al.* [20] elucidate an instantaneous energy partition for a well-deformed sheet as $E_{\rm k,d}/E_{\rm k,cm}(t) = \dot{R}(t)^2/(2U^2)$. Extrapolating this equation to the onset of the impact at $t = 0$

gives

$$\frac{E_{\rm k,d}}{E_{\rm k,cm}} = \frac{\dot{R}_0^2}{2U^2}. \tag{B1}$$

Equation (B1) is plotted as a dashed line in Fig. 9. It is shown that with a larger $\dot{R}_0/U$, Eq. (B1) increasingly overestimates the energy partition from our simulation. This
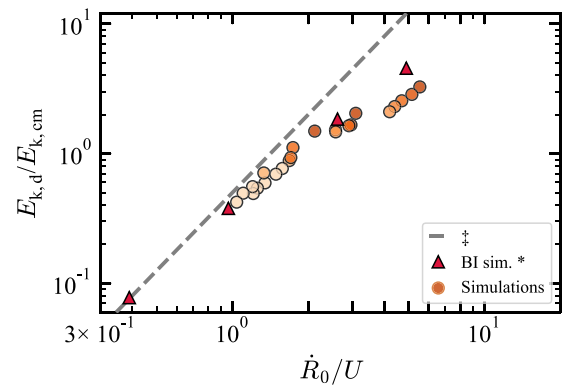

FIG. 9. Simulated kinetic energy partition $E_{\rm k,d}/E_{\rm k,cm}$ as a function of the velocity ratio $\dot{R}_0/U$. The simulation data shown here as orange circles correspond to those of Fig. 7. The dashed line ‡ was calculated using Eq. (B1), as proposed by Gelderblom *et al.* in Ref. [20].

discrepancy might in part be due to a more curved sheet shape when employing a tighter laser beam (see Fig. 2 and the discussion in Sec. II A), leading to a larger deviation of the target morphology from the assumption of a uniform sheet. We also plot the results of boundary integral (BI) simulations extracted from Ref. [20] (red triangles).

[1] V. Bakshi (ed.), *EUV Lithography*, 2nd ed. (SPIE Press, Bellingham, 2018).

[2] Y. Tao, J. T. Stewart, J. Jur, A. LaForge, D. Brown, M. J. Arcand, A. A. Schafgans, and M. A. Purvis, Extreme ultraviolet light source, ASML Netherlands B.V., U.S. Patent No. 20160007434A1, 2016.

[3] M. Purvis, I. V. Fomenkov, A. A. Schafgans, P. Mayer, K. Hummler, M. H. Leenders, Y. Tao, S. I. Rokitski, J. Stewart, A. I. Ershov, R. J. Rafac, S. D. Dea, G. O. Vaschenko, D. C. Brandt, and D. J. Brown, Laser-produced plasma incoherent EUV light sources for high-volume manufacturing semiconductor lithography (conference presentation), in *X-Ray Lasers and Coherent X-Ray Sources: Development and Applications XIII*, Proc. SPIE, Vol. 11111, edited by A. Klisnick and C. S. Menoni (SPIE, San Diego, 2019).

[4] O. O. Versolato, Physics of laser-driven tin plasma sources of EUV radiation for nanolithography, Plasma Sources Sci. Technol. **28**, 083001 (2019).

[5] T. Sizyuk and A. Hassanein, Tuning laser wavelength and pulse duration to improve the conversion efficiency and performance of EUV sources for nanolithography, Phys. Plasmas **27**, 103507 (2020).

[6] I. Fomenkov, D. Brandt, A. Ershov, A. Schafgans, Y. Tao, G. Vaschenko, S. Rokitski, M. Kats, M. Vargas, M. Purvis, R. Rafac, B. La Fontaine, S. De Dea, A. LaForge, J. Stewart, S. Chang, M. Graham, D. Riggs, T. Taylor, M. Abraham *et al.*, Light sources for high-volume manufacturing EUV lithography: Technology, performance, and power scaling, Adv. Opt. Technol. **6**, 173 (2017).

[7] S. Churilov and A. Ryabtsev, Analysis of the spectra of In XII–XIV and Sn XIII–XV in the far-VUV region, Opt. Spectrosc. **101**, 169 (2006).

[8] A. Ryabtsev, É. Y. Kononov, and S. Churilov, Spectra of rubidium-like Pd X–Sn XIV ions, Opt. Spectrosc. **105**, 844 (2008).

[9] G. O'Sullivan, B. Li, R. D'Arcy, P. Dunne, P. Hayden, D. Kilbane, Tom McCormack, H. Ohashi, F. O'Reilly, P. Sheridan, E. Sokell, C. Suzuki, and Takeshi Higashiguchi, Spectroscopy of highly charged ions and its relevance to EUV and soft x-ray source development, J. Phys. B: At., Mol. Opt. Phys. **48**, 144025 (2015).

[10] F. Torretti, J. Sheil, R. Schupp, M. Basko, M. Bayraktar, R. Meijer, S. Witte, W. Ubachs, R. Hoekstra, O. O. Versolato *et al.*, Prominent radiative contributions from multiply-excited states in laser-produced tin plasma for nanolithography, Nat. Commun. **11**, 2334 (2020).

[11] J. Scheers, C. Shah, A. Ryabtsev, H. Bekker, F. Torretti, J. Sheil, D. A. Czapski, J. C. Berengut, W. Ubachs, J. R. C. López-Urrutia, R. Hoekstra, and O. O. Versolato, EUV spectroscopy of highly charged Sn^{13+}–Sn^{15+} ions in an electron-beam ion trap, Phys. Rev. A **101**, 062511 (2020).

[12] J. Sheil, O. O. Versolato, A. J. Neukirch, and J. Colgan, Multiply-excited states and their contribution to opacity in CO_2 laser-driven tin-plasma conditions, J. Phys. B: At., Mol. Opt. Phys. **54**, 035002 (2021).

[13] S. Fujioka, M. Shimomura, Y. Shimada, S. Maeda, H. Sakaguchi, Y. Nakai, T. Aota, H. Nishimura, N. Ozaki, A. Sunahara, K. Nishihara, N. Miyanaga, Y. Izawa, and K. Mima, Pure-tin microdroplets irradiated with double laser pulses for efficient and minimum-mass extreme-ultraviolet light source production, Appl. Phys. Lett. **92**, 241502 (2008).

[14] H. Mizoguchi, T. Abe, Y. Watanabe, T. Ishihara, T. Ohta, T. Hori, A. Kurosu, H. Komori, K. Kakizaki, A. Sumitani, O. Wakabayashi, H. Nakarai, J. Fujimoto, and A. Endo, First generation laser-produced plasma source system for HVM EUV lithography, Proc. SPIE **7636**, 763608 (2010).

[15] V. Y. Banine, K. N. Koshelev, and G. H. P. M. Swinkels, Physical processes in EUV sources for microlithography, J. Phys. D **44**, 253001 (2011).

[16] E. Louis, A. Yakshin, T. Tsarfati, and F. Bijkerk, Nanometer interface and materials control for multilayer EUV-optical applications, Prog. Surf. Sci. **86**, 255 (2011).

[17] D. J. Hemminga, L. Poirier, M. M. Basko, R. Hoekstra, W. Ubachs, O. O. Versolato, and J. Sheil, High-energy ions from Nd:YAG laser ablation of tin microdroplets: Comparison between experiment and a single-fluid hydrodynamic model, Plasma Sources Sci. Technol. **30**, 105006 (2021).

[18] A. L. Klein, W. Bouwhuis, C. W. Visser, H. Lhuissier, C. Sun, J. H. Snoeijer, E. Villermaux, D. Lohse, and H. Gelderblom, Drop Shaping by Laser-Pulse Impact, Phys. Rev. Appl. **3**, 044018 (2015).

[19] D. Kurilovich, A. L. Klein, F. Torretti, A. Lassise, R. Hoekstra, W. Ubachs, H. Gelderblom, and O. O. Versolato, Plasma Propulsion of a Metallic Microdroplet and Its Deformation upon Laser Impact, Phys. Rev. Appl. **6**, 014018 (2016).

[20] H. Gelderblom, H. Lhuissier, A. L. Klein, W. Bouwhuis, D. Lohse, E. Villermaux, and J. H. Snoeijer, Drop deformation by laser-pulse impact, J. Fluid Mech. **794**, 676 (2016).

[21] D. Kurilovich, M. M. Basko, D. A. Kim, F. Torretti, R. Schupp, J. C. Visschers, J. Scheers, R. Hoekstra, W. Ubachs, and O. O. Versolato, Power-law scaling of plasma pressure on laser-ablated tin microdroplets, Phys. Plasmas **25**, 012709 (2018).

[22] B. Liu, R. A. Meijer, J. Hernandez-Rueda, D. Kurilovich, Z. Mazzotta, S. Witte, and O. O. Versolato, Laser-induced vaporization of a stretching sheet of liquid tin, J. Appl. Phys. **129**, 053302 (2021).

[23] B. Liu, D. Kurilovich, H. Gelderblom, and O. O. Versolato, Mass Loss from a Stretching Semitransparent Sheet of Liquid Tin, Phys. Rev. Appl. **13**, 024035 (2020).

[24] M. M. Basko, V. G. Novikov, and A. S. Grushin, On the structure of quasi-stationary laser ablation fronts in strongly radiating plasmas, Phys. Plasmas **22**, 053111 (2015).

[25] E. Villermaux and B. Bossa, Drop fragmentation on impact, J. Fluid Mech. **668**, 412 (2011).

[26] Y. Wang and L. Bourouiba, Growth and breakup of ligaments in unsteady fragmentation, J. Fluid Mech. **910**, A39 (2021).

[27] A. L. Klein, D. Kurilovich, H. Lhuissier, O. O. Versolato, D. Lohse, E. Villermaux, and H. Gelderblom, Drop fragmentation by laser-pulse impact, J. Fluid Mech. **893**, A7 (2020).

[28] Y. Wang, R. Dandekar, N. Bustos, S. Poulain, and L. Bourouiba, Universal Rim Thickness in Unsteady Sheet Fragmentation, Phys. Rev. Lett. **120**, 204503 (2018).

[29] C. Josserand and S. T. Thoroddsen, Drop impact on a solid surface, Annu. Rev. Fluid Mech. **48**, 365 (2016).

[30] S. Wildeman, C. W. Visser, C. Sun, and D. Lohse, On the spreading of impacting drops, J. Fluid Mech. **805**, 636 (2016).

[31] C. Clanet, C. Béguin, D. Richard, and D. Quéré, Maximal deformation of an impacting drop, J. Fluid Mech. **517**, 199 (2004).

[32] J. Philippi, P.-Y. Lagrée, and A. Antkowiak, Drop impact on a solid surface: Short-time self-similarity, J. Fluid Mech. **795**, 96 (2016).

[33] J. Eggers, M. Fontelos, C. Josserand, and S. Zaleski, Drop dynamics after impact on a solid wall: Theory and simulations, Phys. Fluids **22**, 1063 (2010).

[34] C. W. Visser, P. E. Frommhold, S. Wildeman, R. Mettin, D. Lohse, and C. Sun, Dynamics of high-speed micro-drop impact: Numerical simulations and experiments at frame-to-frame times below 100 ns, Soft Matter **11**, 1708 (2015).

[35] Y. Wang and L. Bourouiba, Drop impact on small surfaces: Thickness and velocity profiles of the expanding sheet in the air, J. Fluid Mech. **814**, 510 (2017).

[36] Y. Wang *et al.*, Fundamentals in unsteady fluid fragmentation from drop impact, Ph.D. thesis, Massachusetts Institute of Technology, 2021.

[37] D. Kurilovich, Laser-induced dynamics of liquid tin microdroplets, Ph.D. thesis, Vrije Universiteit Amsterdam, 2019.

[38] T. de Faria Pinto, J. Mathijssen, R. Meijer, H. Zhang, A. Bayerle, D. Kurilovich, O. O. Versolato, K. S. Eikema, and S. Witte, Cylindrically and non-cylindrically symmetric expansion dynamics of tin microdroplets after ultrashort laser pulse impact, Appl. Phys. A **127**, 93 (2021).

[39] R. A. Meijer, R. Schupp, J. Sheil, M. M. Basko, K. S. E. Eikema, O. O. Versolato, and S. Witte, Spall-Velocity Reduction in Double-Pulse Impact on Tin Microdroplets, Phys. Rev. Appl. **16**, 024026 (2021).

[40] R. Meijer, Tailored laser-droplet interaction: For target formation in extreme ultraviolet sources, Ph.D. thesis, Vrije Universiteit Amsterdam, 2021.

[41] J. Hermens, H. Gelderblom, B. Liu, J. Duffhues, P. Rindt, and O. Versolato, Laser-impact-induced splashing: An analysis of the splash crown evolution after Nd:YAG ns-pulse laser impact on a liquid tin pool, Appl. Phys. B **127**, 44 (2021).

[42] Y. Wang and L. Bourouiba, Unsteady sheet fragmentation: Droplet sizes and speeds, J. Fluid Mech. **848**, 946 (2018).

[43] M. M. Basko, J. Maruhn, and A. Tauschwitz, Development of a 2D radiation-hydrodynamics code RALEF for laser plasma simulations, GSI Report 2010-1, PLASMA-PHYSICS-25, GSI Helmholtzzentrum für Schwerionenforschung GmbH, 2010.

[44] M. M. Basko, P. V. Sasorov, M. Murakami, V. G. Novikov, and A. S. Grushin, One-dimensional study of the radiation-dominated implosion of a cylindrical tungsten plasma column, Plasma Phys. Control. Fusion **54**, 055003 (2012).

[45] A. Tauschwitz, M. Basko, A. Frank, V. Novikov, A. Grushin, A. Blazevic, M. Roth, and J. Maruhn, 2D radiation-hydrodynamics modeling of laser-plasma targets for ion stopping measurements, High Energy Density Phys. **9**, 158 (2013).

[46] S. Faik, A. Tauschwitz, M. M. Basko, J. A. Maruhn, O. Rosmej, T. Rienecker, V. G. Novikov, and A. S. Grushin, Creation of a homogeneous plasma column by means of Hohlraum radiation for ion-stopping measurements, High Energy Density Phys. **10**, 47 (2014).

[47] M. M. Basko, On the maximum conversion efficiency into the 13.5-nm extreme ultraviolet emission under a steady-state laser ablation of tin microspheres, Phys. Plasmas **23**, 083114 (2016).

[48] M. M. Basko, M. S. Krivokorytov, A. Y. Vinokhodov, Y. V. Sidelnikov, V. M. Krivtsun, V. V. Medvedev, D. A. Kim, V. O. Kompanets, A. A. Lash, and K. N. Koshelev, Fragmentation dynamics of liquid-metal droplets under ultra-short laser pulses, Laser Phys. Lett. **14**, 036001 (2017).

[49] R. Schupp, L. Behnke, J. Sheil, Z. Bouza, M. Bayraktar, W. Ubachs, R. Hoekstra, and O. O. Versolato, Characterization of 1- and 2-μm wavelength laser-produced microdroplet-tin plasma for generating extreme-ultraviolet light, Phys. Rev. Research **3**, 013294 (2021).

[50] F. L. Addessio, J. R. Baumgardner, J. K. Dukowicz, N. L. Johnson, B. A. Kashiwa, R. M. Rauenzahn, and C. Zemach, CAVEAT: A computer code for fluid dynamics problems with large distortion and internal slip, Report No. LA-10613-MS-Rev. 1, UC-32, Los Alamos National Laboratory, 1992.

[51] E. Livne and A. Glasner, A finite difference scheme for the heat conduction equation, J. Comput. Phys. **58**, 59 (1985).

[52] M. Basko, J. Maruhn, and A. Tauschwitz, An efficient cell-centered diffusion scheme for quadrilateral grids, J. Comput. Phys. **228**, 2175 (2009).

[53] A. Dedner and P. Vollmöller, An adaptive higher order method for solving the radiation transport equation on unstructured grids, J. Comput. Phys. **178**, 263 (2002).

[54] J. I. Castor, Radiation hydrodynamics, Tech. Rep. (Lawrence Livermore National Laboratory, Livermore, CA, 2003).

[55] A. F. Nikiforov, V. G. Novikov, and V. B. Uvarov, *Quantum-Statistical Models of Hot Dense Matter: Methods for Computation Opacity and Equation of State*, Progress in Mathematical Physics (Birkhauser, Basel, 2005).

[56] V. G. Novikov, V. V. Ivanov, K. N. Koshelev, V. M. Krivtsun, and A. D. Solomyannaya, Calculation of tin emission spectra in discharge plasma: The influence of reabsorption in spectral lines, High Energy Density Phys. **3**, 198 (2007).

[57] S. Faik, A. Tauschwitz, and I. Iosilevskiy, The equation of state package FEOS for high energy density matter, Comput. Phys. Commun. **227**, 117 (2018).

[58] R. M. More, K. H. Warren, D. A. Young, and G. B. Zimmerman, A new quotidian equation of state (QEOS) for hot dense matter, Phys. Fluids **31**, 3059 (1988).

[59] A. Kemp and J. M. ter Vehn, An equation of state code for hot dense matter, based on the QEOS description, Nucl. Instrum. Methods Phys. Res., Sect. A **415**, 674 (1998).

[60] M. M. Basko and I. P. Tsygvintsev, A hybrid model of laser energy deposition for multi-dimensional simulations of plasmas and metals, Comput. Phys. Commun. **214**, 59 (2017).

[61] S. A. Reijers, J. H. Snoeijer, and H. Gelderblom, Droplet deformation by short laser-induced pressure pulses, J. Fluid Mech. **828**, 374 (2017).

[62] C. R. Phipps, T. P. Turner, R. F. Harrison, G. W. York, W. Z. Osborne, G. K. Anderson, X. F. Corlis, L. C. Haynes, H. S. Steele, K. C. Spicochi, and T. R. King, Impulse coupling

to targets in vacuum by KrF, HF, and CO_2 single-pulse lasers, J. Appl. Phys. **64**, 1083 (1988).

[63] S. Reijers, Droplet impact phenomena in nanolithography, Ph.D. thesis, University of Twente, Netherlands, 2019.

[64] P. W. Humrickhouse, An equation of state and compendium of thermophysical properties of liquid tin, a prospective plasma-facing material, IEEE Trans. Plasma Sci. **47**, 3374 (2019).

[65] S. A. Reijers, D. Kurilovich, F. Torretti, H. Gelderblom, and O. O. Versolato, Laser-to-droplet alignment sensitivity relevant for laser-produced plasma sources of extreme ultraviolet light, J. Appl. Phys. **124**, 013102 (2018).

[66] D. Hudgins, N. Gambino, B. Rollinger, and R. Abhari, Neutral cluster debris dynamics in droplet-based laser-produced plasma sources, J. Phys. D **49**, 185205 (2016).